A Pulse Frequency Modulation Interpretation of VCOs Enabling VCO-ADC Architectures With Extended Noise Shaping

Eric Gutierrez, *Student Member, IEEE*, Luis Hernandez, *Member, IEEE*, Fernando Cardes, and Pieter Rombouts, *Member, IEEE*

Abstract—In this paper, we propose to study voltage controlled oscillators (VCOs) based on the equivalence with pulse frequency modulators (PFMs). This approach is applied to the analysis of VCO-based analog-to-digital converters (VCO-ADCs) and deviates significantly from the conventional interpretation, where VCO-ADCs have been described as the first-order $\Delta\Sigma$ modulators. A first advantage of our approach is that it unveils systematic error components not described by the equivalence with a conventional $\Delta\Sigma$ modulator. A second advantage is that, by a proper selection of the pulses generated by the PFM, we can theoretically construct an open loop VCO-ADC with an arbitrary noise shaping order. Unfortunately, with the exception of the first-order noise shaping case, the required pulse waveforms cannot easily be implemented on the circuit level. However, we describe circuit techniques to achieve a good approximation of the required pulse waveforms, which can easily be implemented by practical circuits. Finally, our approach enables a straightforward description of multistage $\Delta\Sigma$ modulator architectures, which is an alternative and practically feasible way to realize a VCO-ADC with extended noise shaping.

Index Terms— $\Delta\Sigma$ modulation, data conversion, voltage controlled oscillators, pulse frequency modulation, time encoding.

I. Introduction

THE possibility of encoding an analog signal with a voltage controlled oscillator (VCO) has been around since the beginning of electronics. Ideally, a VCO produces a linear voltage-to-frequency conversion that may be encoded into a square wave of digital nature. In the past, such VCOs were used in instrumentation and radiocommunication applications to transmit analog signals in noisy environments. In [1] and [2], it was shown that a VCO could be used to perform first order noise shaped analog-to-digital conversion. In its simplest form, a VCO-based analog-to-digital converter (VCO-ADC) can be implemented with the circuit of Fig. 1(a), which requires very few components (apart from the VCO). Moreover, these components are fully digital.
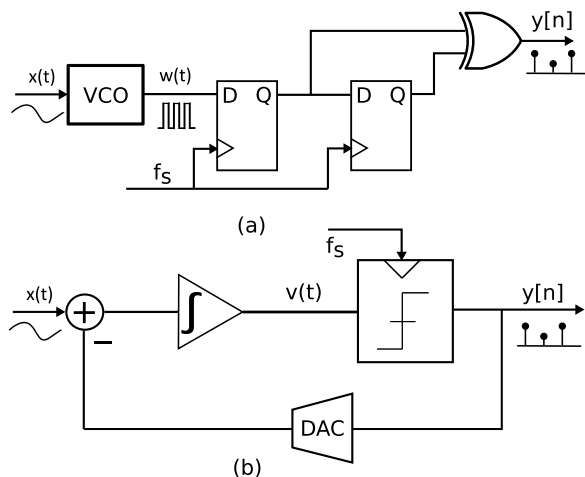
Fig. 1. Equivalent systems: (a) VCO-ADC, (b) continuous time $\Delta\Sigma$ modulator.

For some time, VCO-ADCs were not very popular due to the availability of competing analog linear circuits, which allowed the implementation of efficient data converters [3]. For this reason, VCO-ADCs were mainly targeted for ultra low power applications or sensors [4], [5]. However, poor analog performance and low supply voltages in nanometer technologies demand new data conversion paradigms. Here, the VCO-ADC architecture is a promising candidate.

One of the most interesting implementations of VCO-ADCs makes use of ring oscillators (ROs) [4], [6]–[8], which only require digital circuitry. In the past, the main problem that prevented the widespread use of RO-based VCO-ADCs, was considered to be nonlinearity [6]. By now, a large amount of research was performed on nonlinearity compensation, and today many solutions to tackle the linearity problem have been published, e.g. [9]–[16]. However, although some high order noise shaping VCO-ADCs have been published [17]–[22], a systematic design methodology of VCO-ADCs with arbitrary noise shaping order is still missing. The contribution of this manuscript is on this frontier.

The initial analyses of VCO-ADCs tried to explain the operation of Fig. 1(a) with linear time-domain equations. In [6], [23], and [24], to name a few, the circuit of Fig. 1(a) was shown to behave as the continuous time first order $\Delta\Sigma$ modulator shown on Fig. 1(b). The equivalence is based on considering the phase of the oscillator $\Phi(t)$ as the state variable of an integrator ($v(t)$ in Fig. 1(b)). This interpretation is restricted by the need to approximate the quantization error, which is typically assumed to be white noise. Based on
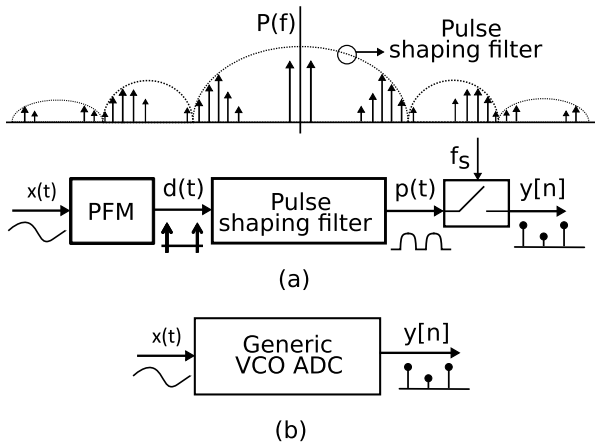
Fig. 2.   Approach followed: from the (a) PFM + pulse shaping filter + sampler architecture to a (b) generic order VCO-ADC structure.

Fig. 3.   VCO – PFM equivalence.

this model, VCO-ADCs were considered part of the $\Delta\Sigma$ ADC family and their description was as accurate as the conventional $\Delta\Sigma$ theory (and hence restricted by the model of the quantization error). Although the white noise model is useful to understand practical circuits, it is obviously an approximation and does not explain the true spectral structure of quantization noise or modulator stability. Several efforts have been made to refine the white noise model [25], [26], but most of them still use statistics. In [27] and [28], an equivalence between a $\Delta\Sigma$ modulator and a FM modulator was first identified. Building forth on [27], exact analytical expressions for the output spectrum of a VCO-ADC were calculated in [29]. The key element of this analysis is to model the VCO-ADC as a pulse frequency modulator (PFM) combined with a sampler. This approach brings new insight, because the spectrum of a PFM signal can be described by a trigonometric series [30]. This gives us the opportunity to reformulate the description of VCO-ADCs in an analytical way and answer the questions left aside by conventional $\Delta\Sigma$ modulation theory.

The main target of this paper is to extend the mathematical foundations of [29] and to derive new VCO-based data converter architectures. Our approach is different from prior work on VCO-ADC architectures such as [18]–[22], where the integrators in the loop filter of a continuous time $\Delta\Sigma$ modulator are replaced by VCO-based equivalents and therefore require a feedback loop. Instead, we will concentrate on open loop architectures with no feedback around the VCOs [31].

The approach that we will follow is depicted in Fig. 2. Based on the PFM interpretation, we will propose a generic architecture of a VCO-ADC which consists of a PFM followed by a pulse shaping filter and a sampler (Fig. 2(a)). The spectral characteristics of the pulse shaping filter will permit to tailor the noise shaping of the VCO-ADC (Fig. 2(b)). The well known circuit of Fig. 1(a) will turn out to be a particular case of this generic architecture, implementing first order noise shaping. As will become clear, the approach enables a straightforward extension toward VCO-based multistage architectures (MASH), which is an alternative way to extend the noise shaping order.

The paper is organized in two main parts. The first part discusses the theoretical foundations of this new way of explaining VCO-ADCs and is developed in Sections II and III. The second part discusses two application examples of the previous theory and is developed in Sections IV and V. In more detail, Section II reviews the classical analysis of
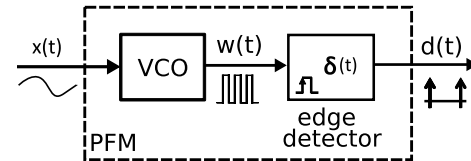
a VCO-ADC based on the phase-frequency relationship and introduces the alternative interpretation based on the PFM. The PFM interpretation reveals a systematic error present in all VCO-ADCs that had not been identified previously. In Section III, the theory developed in Section II is applied to build a generic VCO-ADC architecture with extended noise shaping order, based on a PFM block followed by a pulse shaping linear filter. Although direct higher order VCO-ADC architectures are not easily implementable, we explore in Section IV some approximations based on an analog finite impulse response (FIR) filter. Section V focuses on generalizing the theory proposed in Section III to the implementation of MASH structures. Finally, Section VI concludes the paper.

II. PULSE FREQUENCY MODULATION: AN ALTERNATIVE WAY TO LOOK AT A VCO

In this section we will review how a VCO can be used for the coding of a continuous-time analog signal. For this purpose, we will show that there is a strict equivalence between the VCO operation and pulse frequency modulation. This is a modulation technique that encodes band-limited signals into a train of Dirac delta impulses, where the information is encoded in the time position of the impulses [32].

A. VCO – PFM Equivalence

Fig. 3 shows a VCO and the associated PFM signals. Here, the input signal $x(t)$ drives a VCO and generates the VCO output signal $w(t)$. Without loss of generality, we will assume that the input signal $x(t)$ is bounded to the interval [-1,1], band-limited to a finite bandwidth BW and dimensionless. We will assume that the waveform of $w(t)$ is a square wave. The actual instantaneous VCO frequency is $f(t)$. When looking at the waveform $w(t)$, we see that all the information is contained in the edges of $w(t)$. In our treatment we will assume that only the rising edges are used.[1] If we call the VCO rest frequency f_o (corresponding to a zero input $x = 0$) and the VCO gain K_{VCO}, then the VCO instantaneous frequency $f(t)$ and the instantaneous phase $\Phi(t)$ can be described as follows:

$$f(t) = f_o + K_{VCO} \cdot x(t), \qquad |K_{VCO}| \leq f_o$$

$$\Phi(t) = \int_0^t (f_o + 2\pi K_{VCO} \cdot x(\tau)) \, d\tau$$

$$= 2\pi f_o t + 2\pi K_{VCO} \cdot \int_0^t (x(\tau)) \, d\tau \qquad (1)$$

Note that the VCO gain (K_{VCO}) in this model is a design parameter. However, with our definition of the valid signal range, its value must be bounded as indicated in (1). We will restrict $x(t)$ to have zero mean for notational convenience. This requirement does not pose any practical limitation because

---

[1]Note that the theory remains valid for circuits that use both the rising and the falling edges, but in that case it is more convenient to work with an *effective* VCO frequency $f_{eff}(t)$ which equals twice the actual VCO frequency $f_{eff}(t) = 2f(t)$. This is e.g. the case for the circuit of Fig. 1(a).

if $x(t)$ has a DC component, we can always modify f_o to compensate the frequency offset produced by the DC shift. The rising edges of $w(t)$ represent the crossings of $\Phi(t)$ over integer multiples of 2π. Now, we will generate an auxiliary signal $d(t)$ composed of Dirac delta functions coincident with the rising edges of $w(t)$. For this purpose, we have added the conceptual block "edge detector" to Fig. 3. Mathematically, this leads to:

$$d(t) = \sum_{k=0}^{\infty} \delta(t - t_k), \quad \forall t_k \, |\Phi(t_k) = 2\pi k \, , k = 0, 1, \dots \quad (2)$$

The signal $d(t)$ is a pulse frequency modulated signal [30]. Clearly, this $d(t)$ is a conceptual signal that cannot exist in reality. In practical applications, a pulse frequency modulated signal could be approximated by a train of narrow square pulses. However, for our purposes, it is more convenient to build the argument on the (theoretical) Dirac delta pulse frequency modulated signal $d(t)$.

For a sinusoidal input $x(t)$, the signal $d(t)$ can be expanded into a trigonometric series [29], [30], [33]. It can be shown that $d(t)$ contains modulation sidebands at each multiple of the VCO rest frequency f_o, similarly to a frequency modulated signal. However, it also contains the actual signal $x(t)$ in the baseband, which is different from conventional frequency modulation (FM). If we consider a sinusoidal input signal $x(t)$:

$$x(t) = A \cdot \cos(2\pi f_x t), \quad (3)$$

the signal $d(t)$ can be expanded into a trigonometric series as follows [33]:

$$d(t) = f_o + K_{\text{VCO}} \cdot A \cdot \cos\left(2\pi f_x t\right) + m(t)$$

$$m(t) = 2f_o \sum_{q=1}^{\infty} \sum_{r=-\infty}^{\infty} J_r \left(q \frac{A K_{\text{VCO}}}{f_x} \right)$$

$$\times \left(1 + \frac{r f_x}{q f_o} \right) \cos\left(2\pi \left(q f_o + r f_x\right) t\right) \quad (4)$$

Here J_r is the r-th order Bessel function of the first kind. The expansion (4) can also be represented in the frequency domain by its Fourier transform $D(f)$:

$$D(f) = f_o \delta(f) + \frac{A K_{\text{VCO}}}{2} \left(\delta(f + f_x) + \delta(f - f_x) \right) + M(f)$$

$$M(f) = f_o \sum_{q=1}^{\infty} \sum_{r=-\infty}^{\infty} J_r \left(q \frac{A K_{\text{VCO}}}{f_x} \right) \left(1 + \frac{r f_x}{q f_o} \right)$$

$$\cdot \left(\delta(f + (q f_o + r f_x)) + \delta(f - (q f_o + r f_x)) \right) \quad (5)$$

According to (4) and (5), the signal $d(t)$ consists of a component which is linear with respect to the input signal as well as modulation sidebands components around each harmonic of the VCO rest frequency f_o. These modulation sideband components are denoted by the symbol $m(t)$ (or the associate spectrum $M(f)$).

B. Discussion of the Modulation Spectra

Unfortunately the expression for the spectrum $M(f)$ of the modulation sidebands is not intuitive, because the modulation tones depend in a complex way on the signal parameters (input signal frequency as well as input amplitude). E.g. the sidebands are definitely not symmetrical around the central carrier and also they are not monotonically decaying.
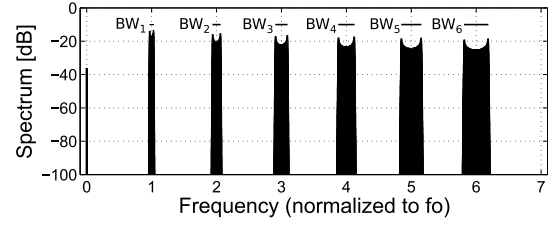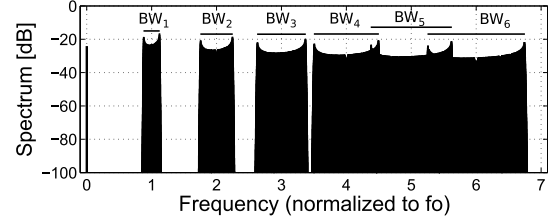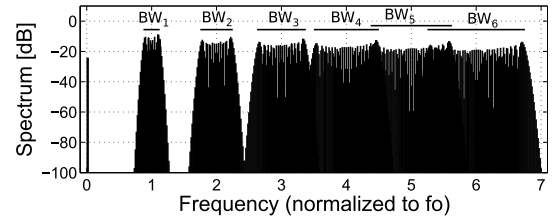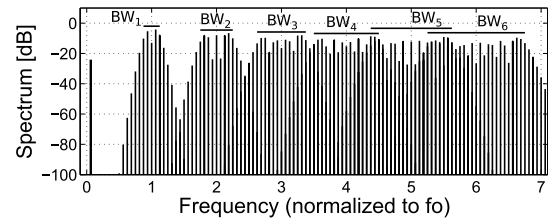

Fig. 4. Calculated spectrum according to (5) of the first six sidebands for the case of an input signal with (a) a low input frequency $f_x = f_o/1024$ and a small input amplitude $A K_{\text{VCO}} = f_o/32$, (b) again for a low input frequency $f_x = f_o/1024$ but a larger input amplitude $A K_{\text{VCO}} = f_o/8$, (c) for the same input amplitude $A K_{\text{VCO}} = f_o/8$ but now an intermediate input frequency $f_x = f_o/64$ and (d) for again the same input amplitude $A K_{\text{VCO}} = f_o/8$ but now a relatively high input frequency $f_x = f_o/16$.

However in general each modulation sideband, roughly consists of a relatively pronounced central lobe and a tail which decays relatively rapidly. This is particularly the case when the input signal frequency f_x is small relative to the VCO rest frequency f_o. This situation is shown in Figs. 4(a) and 4(b) which show the calculated spectrum of the first six sidebands for the case of a low input signal frequency $f_x = f_o/1024$ and two different values of the input amplitude. Although according to (5) in principle, the sidebands around every harmonic of f_o stretch infinitely, it is clear from the figure that the bulk of every sideband's energy is contained in the central lobe which has a limited bandwidth. Moreover, if we denote the value of this limited bandwidth for the qth sideband as BW_q, we found that the following empiric relationship approximately holds:

$$BW_q \approx 2q A K_{\text{VCO}} \quad (6)$$

The corresponding value of the calculated sideband bandwidth is also added to Fig. 4, and it is clear that it matches relatively well for this case of a low input signal frequency
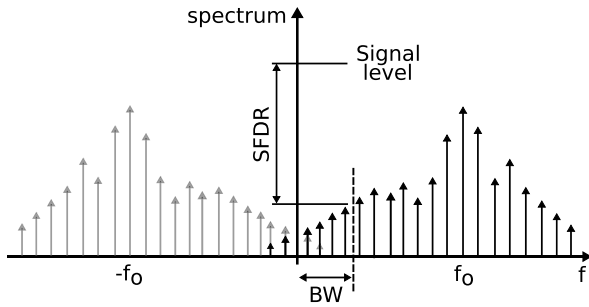
Fig. 5. Sketch of the signal integrity degradation due to spurious tones of the first modulation sideband extending into the useful signal band.

Fig. 6. SNDR due to to the encoding error calculated according to Eq. (7) vs. the input signal frequency f_x for the case of an in input amplitude of -3 dB$_{FS}$ for a fixed bandwidth equal to $f_o/32$.

$f_x = f_o/1024$. As the equation indicates, the higher sidebands become wider, which has the consequence that the spectra of these higher order sidebands (e.g. for $q \geq 4$ in Figs. 4(b)) start to overlap. Due to this, the high frequency spectrum starts to look like white noise.

If we now keep the input amplitude the same as Fig. 4(b), i.e. $AK_{VCO} = f_o/8$, but increase the input frequency to an intermediate value of $f_x = f_o/64$, see Fig. 4(c), we can still distinguish a central lobe with a bandwidth which still follows (6), but the tail of the modulation band decreases much less rapidly. And if we from here further increase the input frequency to a relatively high input frequency of $f_x = f_o/16$, see Fig. 4(d), the tail and the central lobe cannot really be distinguished anymore and the modulation band stretches well beyond the bounds of (6).

C. Fundamental SNDR Limit in VCO-Based Coders

Regardless of the input signal, we can always say that globally, the sideband tones decrease in amplitude when they are further away from the corresponding harmonic of the VCO carrier. However, regardless of how rapidly the tail of each modulation sideband decays, it in reality stretches infinitely far, which means that there are always nonzero sideband tones from the first sideband ($q = 1$ in (4)) that will fall into the useful signal band (BW). This phenomenon is sketched in Fig. 5. In theory there are also contributions from the higher harmonic sidebands, but in practice these are normally negligible compared to those from the first sideband.

The typical decimation filter applied to recover the output data from a VCO-ADC architecture is a low-pass filter. Therefore, although the spectrum of $m(t)$ is deterministic, the in-band sideband tones of Fig. 5 degrade the signal integrity in a similar way as additive noise (or distortion). Then, for a given BW, we can estimate the Signal-to-Noise-and-Distortion Ratio (SNDR) from (5) by summing the contributions of all the components falling into BW:

$$\text{SNDR} = 10\log_{10} \frac{\left(\frac{AK_{VCO}}{2f_o}\right)^2}{\sum_{r=r_{min}}^{r_{max}} \left(J_r(\frac{AK_{VCO}}{f_x})\left(1 + r\frac{f_x}{f_o}\right)\right)^2},$$

$$r_{min} = ceil\left(\frac{-BW - f_o}{f_x}\right), \quad r_{max} = floor\left(\frac{BW - f_o}{f_x}\right)$$
(7)

Here r_{min} and r_{max} correspond to the index of the lowest and the highest component respectively that fall into BW. This equation can be considered as a fundamental encoding error,
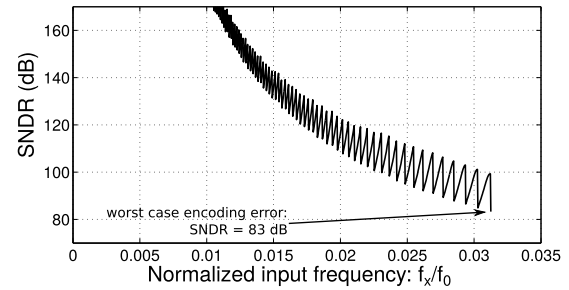
which is inherent in any VCO based scheme, where the VCO encodes the information into the edge positions.

Unfortunately, (7) is again a non intuitive function that depends on the effective amplitude AK_{VCO}, the input signal frequency f_x, the bandwidth BW and the oscillation rest frequency f_o. Upon investigation, this function was found to have a non-monotonic behavior in terms of these parameters. To illustrate this the result for the case of a fixed f_o, a fixed bandwidth $BW = f_o/32$ and a fixed effective input amplitude $AK_{VCO} = f_o/\sqrt{2}$ corresponding to -3 dB$_{FS}$, was evaluated for all inband values of the input frequency f_x (i.e. f_x ranging from DC to the band edge). The resulting SNDR (corresponding to the VCO encoding error) is shown in Fig. 6, and clearly it is a very strong function of the input frequency which is consistent with Fig. 4, where we have already seen that the sideband tones decay much more rapidly for lower frequency input signals. Although for most in band values of the input frequency, the SNDR corresponding to a fundamental encoding error is absurdly high, there are some values for the input frequency (located at the band edge), where the SNDR is much less good and the corresponding worst case here is 83 dB. Since, even in a bandwidth limited application, it is not known in advance what the input frequency will be, this worst case, corresponds to a fundamental SNDR limit.

To further assess this a further study was performed, where the rest oscillation frequency f_o was kept fixed and the signal bandwidth BW was varied. For every value of BW, the input signal frequency f_x was varied in steps of $BW/1000$. Then, (7) was evaluated and the value of the SNDR was collected (leading to a plot such as Fig. 6). Now the worst case SNDR was defined as the fundamental SNDR limit corresponding to this normalized bandwidth value. This procedure was repeated for decreasing values of the input amplitude (starting from absolute full scale, i.e. $A = 1$ going down to -10 dBFS in steps of 1 dB). The results are shown in Fig. 7. The VCO-gain K_{VCO} was set to its maximal value, i.e. $K_{VCO} = f_o$, but it should be noted that the results shown in the figure can be mapped to other values of K_{VCO}, by adjusting the value of the input signal amplitude.

The plot of Fig. 7 is a fundamental performance limit that occurs in all VCO-based coding schemes. As the plot indicates, the performance (set by this hard limit) rapidly increases when the VCO center frequency increases. However, for signals that are really full-scale, the performance increases only very slowly. An important remark is, that this result was derived for a single-phase VCO that only uses the rising edge information. Below, in Section III-C, we will see that the result is also valid for multiphase VCOs (with M phases) that use both the rising and falling edges, provided that we use the
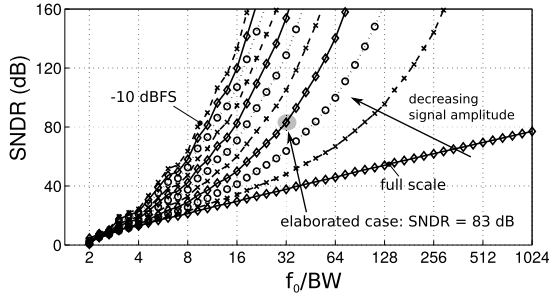
Fig. 7.   Limiting SNDR for the case of an in band input tone vs the ratio f_o/BW for different values of the input signal magnitude (ranging from full scale to -10 dBFS in steps of 1 dB).
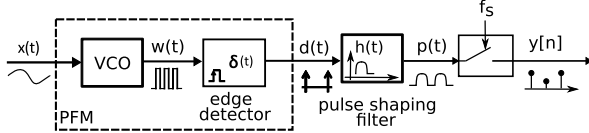

Fig. 8.   Generic structure for a potential VCO-ADC.

effective rest frequency $f_{\mathrm{o,eff}} = 2 \cdot M \cdot f_\mathrm{o}$. Most published VCO-ADC designs until today are operated with $f_{\mathrm{o,eff}}/BW$ values of well above 512 [6], [9], [11], [14], [34]. This means that the performance of these designs were never limited by this fundamental limit.

We will see later on that, when sampling is introduced, there will be additional noise/distortion components which, in many cases, will be larger than this fundamental limit.

III. Direct Construction of a VCO-ADC Based on the PFM Representation

We will now start from the PFM representation described above and define a strategy to derive a family of theoretically possible VCO-ADC structures. We will see that some of these structures do not translate to a circuit that can be implemented in a simple way. However, we will show that one of the derived solutions is equivalent to the simple circuit of Fig. 1(a). Our derivation will enable a much deeper insight in the spectral and tonal behavior of such ADCs than what can be understood from common explanations. Such first order VCO-ADCs are typically explained by linking the phase of the oscillator to the state variable of a $\Delta\Sigma$ modulator [6], [35], which is then quantized and differentiated. Whereas this prior understanding has proven to be insightful, it is stuck at the white noise approximation of the quantization error and cannot explain the tonal behavior that occurs in reality. Our derivation will overcome this limitation and provide exact results.

A. Going From a PFM Encoder to an ADC

Let us look again at the system of Fig. 3. To derive an ADC from this structure, somewhere *sampling* should be introduced. Clearly, signal $d(t)$ cannot be directly sampled because only the Dirac deltas in $d(t)$ coincident with a sampling instant would be detected. This can also be understood in the frequency domain, because sampling of $d(t)$ would introduce a multitude of uncontrolled aliases into the band of interest, due to the non band limited and non decaying spectrum of $d(t)$ (Fig. 4). This would make the recovery of the input signal impossible. Fig. 8 shows a generic VCO-ADC structure that solves the aliasing problem. In the structure, a linear pulse shaping filter with impulse response $h(t)$ is added after the PFM (of Fig. 3). This filter generates an output signal $p(t)$

which can now be sampled with a uniform sampler with sampling frequency f_s to obtain the overall sampled output signal $y[n]$.

The pulse shaping filter has two requirements. First, it must have a low-pass characteristic to allow the input signal components in $d(t)$ to pass through. Second, it should suppress the modulation sidebands located at frequencies that would alias to the low-pass signal band. This can be achieved by placing periodic zeroes in the frequency response at integer multiples of the sampling frequency (which will alias to the baseband). This way, all the baseband aliased components coming from the modulation sidebands will be spectrally shaped similarly to quantization noise in a conventional $\Delta\Sigma$ modulator. As a difference, such structure would be unconditionally stable. The aliasing process and how it is affected by the low-pass filter is represented in Fig. 9.

A good way to construct a suitable filter $h(t)$ is as a cascade of a low-pass function and a linear combination of delays of the sampling period $T_\mathrm{s} = 1/f_\mathrm{s}$. This linear combination of delays allows to implement the periodic zeroes. A potential solution for this is the $sinc_n$ filter:

$$H_n(s) = sinc_n = \frac{\left(1 - e^{-sT_s}\right)^n}{(sT_s)^n} \qquad (8)$$

In (8), the zeroes of n-th order at $s = 0$ are canceled by the poles of $1/(sT_s)^n$, resulting in a unity gain at DC and a periodic zero structure at integer multiples of the sampling frequency f_s. This filter would spectrally shape the aliases of the modulation sidebands by a n-th order zero, in a similar way as the NTF of an n-th order $\Delta\Sigma$ modulator. Fig. 10 shows the pulse shape and the frequency response for $n = 1$ (the case used also in Fig. 9) and $n = 2$.

B. Error Analysis of the Generic VCO-ADC

Above in Section II.B, we have identified and quantified the first error in any VCO-ADC: i.e. the fundamental PFM encoding error which was illustrated in Fig. 7. Now, we will quantify a second error that occurs in our generic VCO-ADC structure of Fig. 8. For this, we will start with the model shown in Fig. 11(a).

Here $M(s)$ corresponds to the Laplace transform of the modulation terms introduced by the pulse frequency modulation process [e.g. according to (4)]. To simplify the model, the VCO gain K_{VCO} was normalized to unity and the offset contribution corresponding to the VCO rest oscillation f_o was omitted. Within these approximations, this model provides an exact description of the behavior of our generic VCO-ADC. Then in a next step, we use the property that a Z-domain factor of z^{-1} corresponds to a continuous time delay of one sampling period T_s followed by a sampler [36], [37]. This way, we obtain the model of Fig. 11(b), which is still strictly equivalent to the generic VCO-ADC structure.

The second error in our generic ADC occurs due to aliasing of high frequency components of the filtered modulation signal in the sampling process. In order to quantify this, we split the modulation signal $M(s)$ in two components: first we have the low frequency component M_{LF}, below $f_\mathrm{s}/2$. This low-frequency component gives rise to the fundamental PFM encoding error (see Fig. 7). The second component M_{HF} corresponds to the high frequency content in $M(s)$ above $f_\mathrm{s}/2$. This high frequency component passes through the continuous time filter $1/(sT_s)^n$ and is then prone to aliasing. This process is
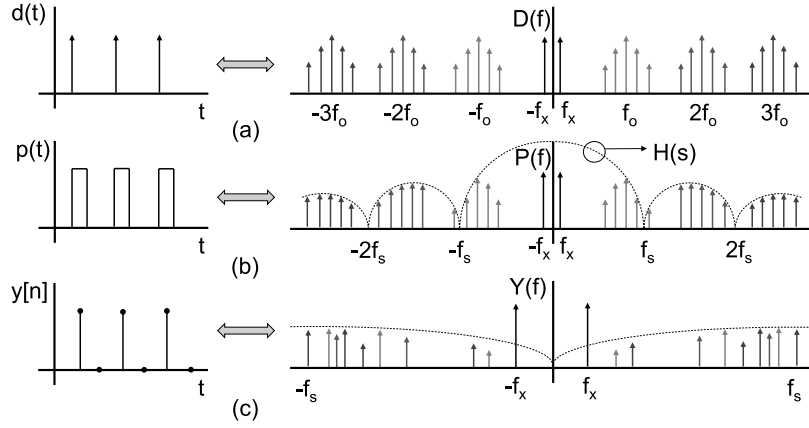
Fig. 9. Illustration of the effect of the lowpass filter $H(s)$ on the aliasing of the modulation sidebands for the case of a single tone sinusoidal input signal, with a sketch of the time domain as well as the frequency domain signals for (a) the signal $d(t)$, (b) the filtered signal $p(t)$ and (c) the sampled overall output signal $y[n]$.
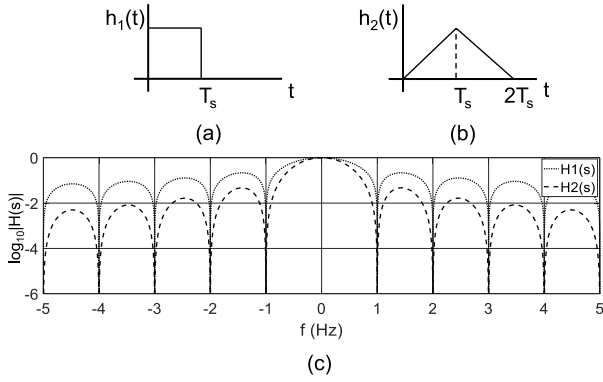

Fig. 10. Time domain impulse response of (a) the first order shaping pulse and and (b) the second order shaping pulse with (c) their respective frequency response.

illustrated in Fig. 11(c), where we reason on the output signal $U(s)$ of the block $1/(sT_s)^n$. Here the two effects of the aliasing phenomenon are modeled explicitly by a combination of two operations: on the one side, the high frequency components U_{HF} of the sampler's input signal U are removed but, on the other side, they re-enter the system again as aliased baseband components which we will denote as U_{al} and which is a discrete time signal. To stress that the aliasing happens in the sampling process we have introduced the special "sampling with aliasing" symbol. If we use the $[\cdot]^*$ operator to indicate sampling as defined in [36], the aliasing error U_{al} is defined as:

$$U_{al} = [U_{HF}]^* \qquad (9)$$

If we assume that the input signal X is band-limited, then the high frequency component U_{HF} is entirely due to the filtered high frequency modulation components $M_{HF}(s)$:

$$U_{HF}(s) = \frac{M_{HF}(s)}{(sT_s)^n} \qquad (10)$$

To emphasize that in this case the aliasing error is entirely due to the VCO's high frequency modulation components, we introduce the symbol M_{al} (read as: the aliased filtered modulation components of the VCO). A similar fact was identified in [38] where the link between quantization noise of a sine wave and frequency modulation was established. In this case M_{al} is equal to the overall aliasing error U_{al}, but we will see below, in Section V, that the aliasing error may consist of multiple components. With these observations, finally our
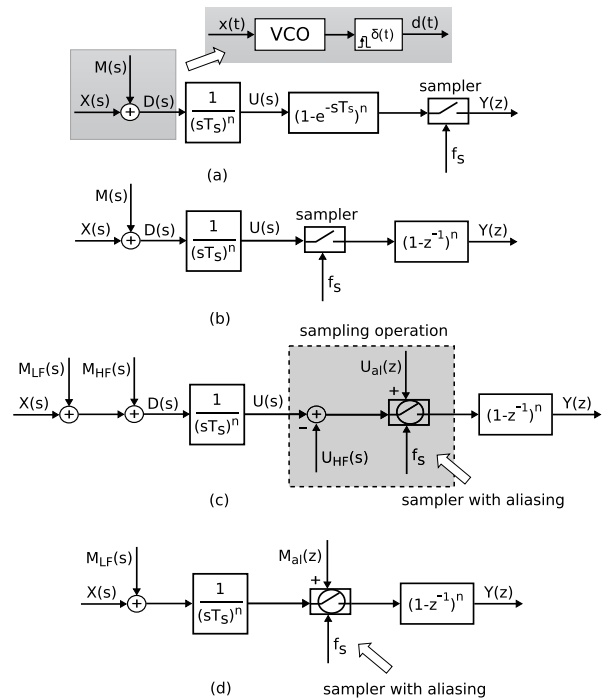
Fig. 11. Explanation of the spectral shaping in our generic VCO-ADC (a) generic VCO-ADC, (b) equivalent structure of our generic VCO-ADC, (c) equivalent structure with explicit indication of the errors in the sampling process, (d) final equivalent model with the overall I/O behavior.

model can be simplified to the model of Fig. 11(d). Now, by inspection, the sampled output $Y(z)$ can be obtained as:

$$Y(z) = \left[\frac{X(s) + M_{LF}(s)}{(sT_s)^n} \right]^* (1 - z^{-1})^n$$
$$+ M_{al}(z)(1 - z^{-1})^n \qquad (11)$$

where the $[\cdot]^*$ operator indicates sampling again. By introducing the signal transfer function STF(s) as:

$$\text{STF}(s) = \frac{(1 - e^{-sT_s})^n}{(sT_s)^n}, \qquad (12)$$

equation (11) can be rewritten as:

$$Y(z) = [\text{STF } X(s)]^*$$
$$+ [\text{STF } M_{LF}(s)]^*$$
$$+ M_{al}(z)(1 - z^{-1})^n \qquad (13)$$

In the above equation, the first term corresponds to the desired signal component. The second term corresponds to the fundamental PFM encoding error (see Section II). The third term corresponds to the aliasing error. As is evident from the equation, this aliasing error will be spectrally shaped according to the order of the pulse shaping filter. Hence, we expect a better SNR for increasing n, but unfortunately (as will be shown later on) it is not obvious to find a practical circuit for the pulse shaper apart from the case where $n = 1$ (first order case).

It should be noted that the aliasing error in this model replaces the quantization error of more conventional phase domain models [6]. However in this model, in principle, the spectra of all the signals in (11) can be calculated exactly. E.g. the spectrum of the aliased signal (which is considered as an error in this system) can be obtained exactly by taking into account the filtering $1/(sT_s)^n$ and then summing over all the aliasing bands of the spectrum of $m(t)$. This closed expression allows the analytical calculation of resulting SNR of $y[n]$ due to the aliases of the modulation sidebands. For the specific case of a zero order hold filter (of first order sinc, $n = 1$), a detailed analytical elaboration of the aliasing process is worked out in [29]. Whereas the theory provides closed analytical expressions for the spectra, the result is still an infinite sum over all the alias bands, which in practice must be numerically approximated with a computer. As a result, these analytical expressions (although of theoretical interest) do not allow neither easy intuition nor hand calculations.

To illustrate the validity of the proposed generic VCO-ADC, we have performed several behavioral simulations according to the conceptual block diagram of Fig. 8, where we have an (ideal) VCO, an edge detector, a pulse shaping filter $H_n(s)$ and a sampler. First, the case where the pulse shaping filter equals the first-order sinc filter $H_1(s)$ was considered. The results of a typical simulation are shown in Fig. 12(a). Here the sampling frequency f_s is arbitrarily set to 1 Hz. The rest frequency f_o of the VCO was set around $f_s/4$: i.e. $f_o \approx f_s/4 = 0.25$ Hz. As before, we have assumed that the VCO input signal $x(t)$ is dimensionless and bounded to the interval $[-1, 1]$. The VCO gain K_{VCO} was set to $K_{VCO} = 0.25$ Hz/unit. The resulting ADC is driven by a sinusoidal input signal with a frequency of $f_s/1024$ and an amplitude of -3 dBFS. The plot clearly demonstrates a 20 dB/dec roll-off, confirming the analysis above. For an OSR of 64, we obtain an SNDR of 51 dB. For comparison, the result of the same experiment but now for the case where the pulse shaping filter equals the second-order sinc filter $H_2(s)$ is shown in Fig. 12(b). As expected, now the spectral roll-off has a slope of 40 dB/dec. The SNDR for an OSR of 64 is now equal to 95 dB. Clearly, in this case, due to the second-order sinc filter, the aliasing error exhibits second order spectral shaping and is greatly suppressed. However, it is important to realize that this spectral shaping only shapes the aliasing error and not the fundamental encoding error discussed in Section II.

For this simulation, the value of the input amplitude, the BW and f_o were chosen such that it corresponds to the case of Fig. 6. Looking back at this figure Fig. 6, we can see that for certain choices of the input frequency f_x (i.e. near band edge), the fundamental encoding error would limit the SNDR to only 83 dB regardless of the spectral shaping of the aliasing error. This is illustrated in Fig. 12(c), which shows the same simulation result as Fig. 12(b) but now for an input frequency f_x near band edge. Now the fundamental encoding
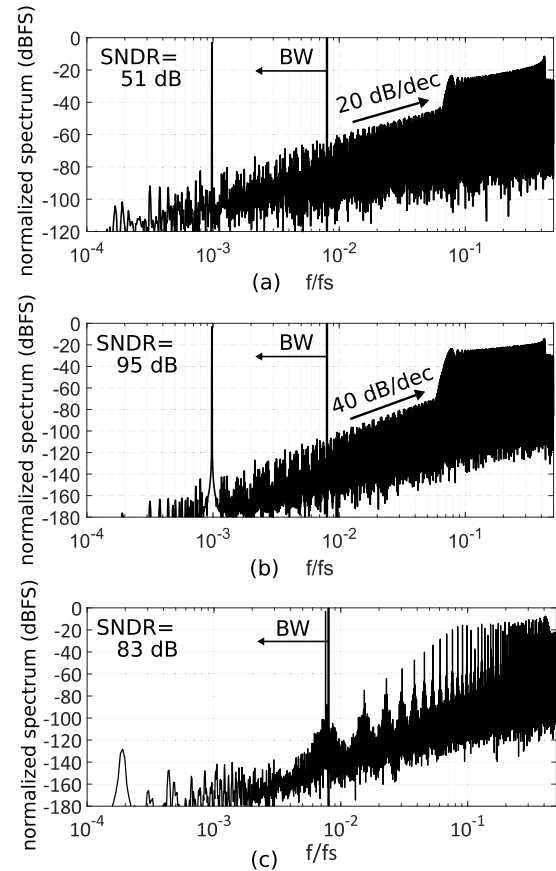

Fig. 12. Output spectra of the generic VCO-ADC architecture illustrating the spectral shaping of the aliasing error for the case of: (a) a first-order sinc filter, (b) a second-order sinc filter, and (c) a second-order sinc filter where the input frequency f_x is chosen such that the SNDR is limited to 83 dB by the fundamental PFM encoding error (i.e. $f_x \approx BW$).

error is larger than the spectrally shaped aliased error and limits the performance to 83 dB, which exactly matches the calculated result shown in Fig. 6.

C. Implementation of a Generic VCO-ADC

Above we have derived a conceptual generic VCO-ADC architecture (Fig. 8). However it is not immediately clear how the continuous-time analog pulse shaping filters should be implemented in practice. In order to investigate this, the time domain waveforms corresponding to the filter's input signal, $d(t)$, and output signal, $p(t)$, are shown in Fig. 13, for the case of the first and second order pulse shaping filters: $H(s) = H_1(s)$ and $H(s) = H_2(s)$, respectively.

In terms of practical implementation, the case with the first order filter is particularly useful. In this case, the impulse response $h_1(t)$ is the standard zero order hold pulse. This enables a hardware efficient realization, because, as shown in Fig. 13(b), the signal $p_1(t)$ will always be composed of discrete amplitude levels due to the constant hold level of the shaping pulse. Then, the sampled signal $y[n]$ would become discrete both in time and in amplitude.

A very interesting situation occurs when the delay between two consecutive pulses in $d(t)$ is larger than or equal to the sampling period $T_s = 1/f_s$. In this case, the filtered signal $p_1(t)$ can only take two possible values ('0 'or '1'). This enables the conceptual realization shown in Fig. 14,
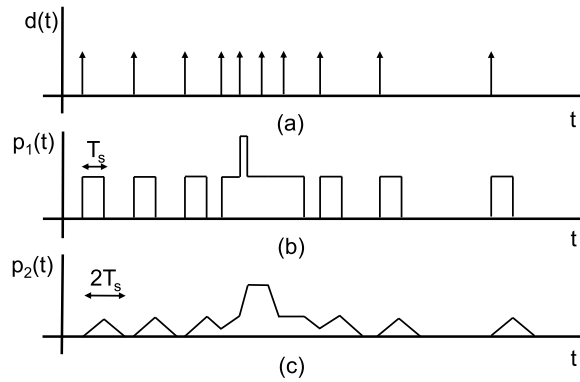
Fig. 13. Time domain waveforms that can occur in the generic VCO structure of Fig. 8: (a) edge signal $d(t)$ (b) output signal $p_1(t)$ of the pulse shaping filter for the first order case and (c) output signal $p_2(t)$ of the pulse shaping filter for the second order case.
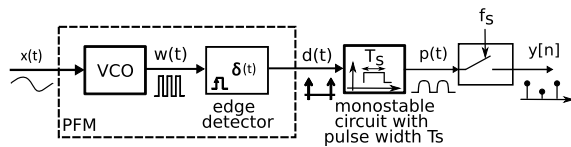

Fig. 14. Conceptual realization of a first order VCO-ADC with a monostable.
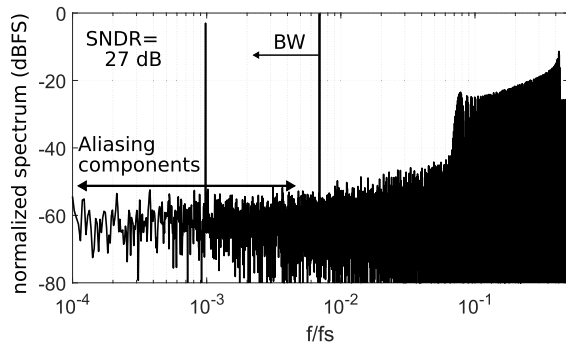

Fig. 15. Performance degradation of the system of Fig. 14 when the length of the pulse in the monostable does not match exactly with T_s (1% deviation).

where the filter is implemented with a monostable which generates a pulse with a width of T_s on every rising edge of the VCO output waveform $w(t)$. Whereas this looks like a viable implementation, it should be noted that this realization is not advised in practice for the following reason: in order to make this circuit operate as desired, the pulse width should perfectly match with the sampling period T_s. In practice this cannot be achieved because mismatch effects that always occur in real circuits will make the pulse length different with respect to the ideal one. From a spectral point of view, this means that the zeroes of the corresponding filter are not exactly placed at integer multiples of the sampling frequency and, as a result, the suppression of the aliasing distortion is much less good than expected. Fig. 15 shows an example of this phenomenon. Here, the system of Fig. 14 was simulated with the same parameters as in Fig. 12, but a monostable whose pulses are only 1% longer in length than the nominal value was used. It can be observed that the performance is completely degraded by the aliasing components, which fall into the bandwidth of the converter and make the SNDR be decreased to 27 dB.

As a difference with the circuit of Fig. 14, the circuit of Fig. 1(a) behaves similarly but automatically forces the sinc filter delay to be coincident with the sampling period [29].
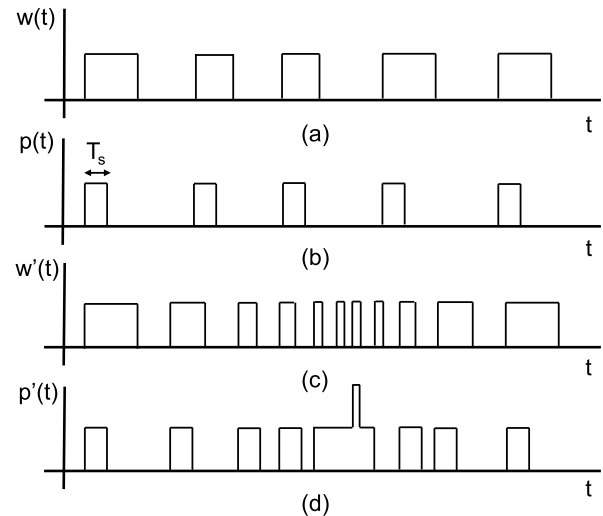

Fig. 16. Effect of sampling frequency in generic first order VCO-ADC when: (14) is accomplished ((a) and (b)); (14) is not accomplished ((c) and (d)).

Therefore, it does not require any matching in the circuit and provides a robust implementation.

By observing Fig. 9 we can see that the model of Fig. 8 does not impose any restriction to the sampling frequency f_s. The spectral shaping of the modulation sidebands would happen regardless of the ratios between f_s, the VCO rest oscillation frequency f_o and the VCO gain K_{VCO}. However, as explained above, the circuit of Fig 1(a) only implements the generic first order VCO-ADC of Fig. 8 if the minimum time distance T_{min} between two edges[2] in the VCO signal $w(t)$ is greater than or equal to the sampling period $T_s = 1/f_s$. Considering a normalized VCO input signal $x(t)$ that is dimensionless and bounded to the interval $[-1, 1]$, we can immediately conclude that the minimum sampling frequency $f_{s,min}$ [6], [35]:

$$f_{s,min} = (f_o + K_{VCO})_{eff} = (f_{max, osc})_{eff} = \left(\frac{1}{T_{min}}\right)_{eff} \quad (14)$$

where $f_{max,osc}$ stands for the highest possible VCO output oscillation frequency.

This can be further understood if we consider the waveforms in the ideal first order case generic VCO-ADC of Fig. 8 for the case where condition (14) is met or not. The situation where the condition is met, is depicted in Fig. 16(a)-(b), where the VCO output $w(t)$ and the corresponding signal $p(t)$ are shown. Now we can see that condition (14) implies that the output signal $p(t)$ obtained from the generic first order VCO-ADC is a single bit signal which is evident from the observation that $p(t)$ has only two voltage levels. By contrast, if $f_{max,osc}$ is higher than the sampling frequency, as in Fig. 16(c)-(d), the output signal $p(t)$ will become a multi-level signal. In this case, we still maintain discrete output signal levels, which can still easily be represented by a digital representation, but now a multi-bit version. This situation in fact corresponds to the behavior of the well known multiphase ring oscillator VCO-ADC of Fig. 17(a). Here each of the M phases of the VCO is connected to the readout circuit of Fig. 1(a) and the overall sampled output signal $y[n]$ is

---

[2]Remember that the circuit of Fig 1(a) reacts both on the rising as well as the falling edges and hence should be analyzed with an effective oscillation frequency f_{eff} equal to twice the actual oscillation frequency.
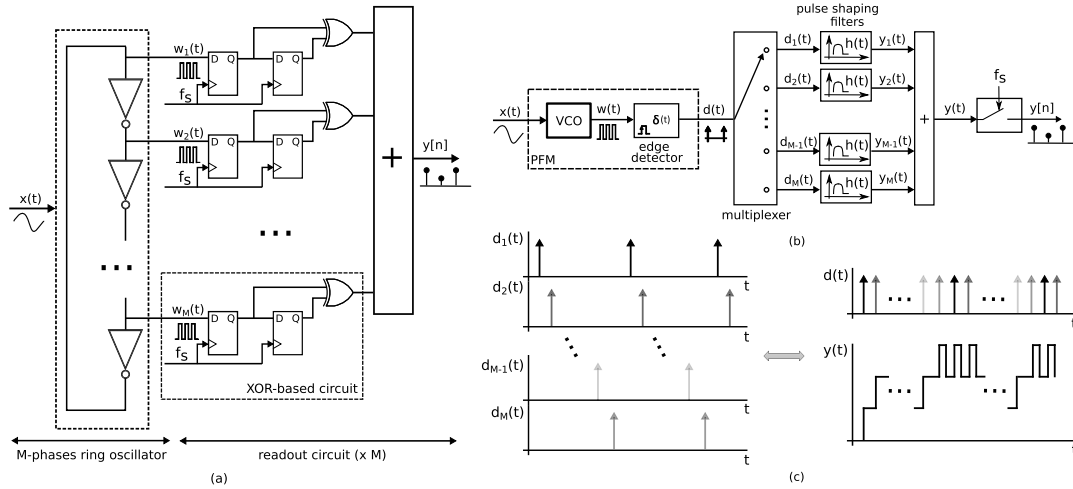
Fig. 17.   Ring oscillator based VCO-ADC concepts: (a) circuit, (b) conceptual diagram, and (c) time chronogram.

obtained as the sum over all the phases in the VCO. Clearly now, the output signal $y[n]$ is a multi level signal. This circuit can also be understood as an implementation of our generic first order VCO architecture with a high effective oscillation frequency f_{eff} given by [6], [35], [39]:

$$f_{\text{eff}} = 2 \cdot M \cdot (f_o + K_{\text{VCO}} \cdot x(t)) \qquad (15)$$

In this case, the effective frequency does not comply with (14) and hence the overall behavior corresponds to Fig. 16(c)-(d).

Fig. 17(b) shows a system level block diagram that describes the behavior of Fig.17(a). In Fig.17(b), a single output PFM is connected to a multiplexer that casts the Dirac delta impulses in $d(t)$ into an array of identical pulse shaping filters. Each time a Dirac delta impulse enters the multiplexer, the switch advances to the next output in a cyclic way, sorting the Dirac delta impulses into M streams (see Fig.17(c)). Every individual Dirac delta stream has a frequency M times lower than f_{eff} and then, (14) will hold. Therefore, each branch can use the circuit based on an XOR gate shown in Fig. 17(a) to implement the sampled pulse shaping filter with no restrictions. The system is exactly equivalent to Fig. 14.

Let us investigate Fig. 13 again, but now for the second order case, i.e. Fig. 13(c). Unfortunately, the pulse does not have a constant level moreover, the pulse values can vary continuously. As a result, at the sampling instants, we would sample a real valued quantity and such a real number cannot easily be represented using digital signals. A similar argument can be made for all orders higher than one. The authors have not found any other filter possessing the same properties as the zero order hold that could allow an exact implementation of a higher noise shaping order ADC. However, high order pulse shapes can be approximated by means of continuous time FIR filters defined by digital delays [40] as will be shown in the next section.

IV. APPROXIMATION OF SECOND ORDER PULSE SHAPING FILTERS WITH A CONTINUOUS TIME FIR FILTER

The ideal triangular impulse response (represented by the filter $h_2(t)$, Fig. 10(b)) is not easily implementable in practice. Nevertheless, we might still think of approximating its impulse response through the staircase shape $h_{2,M}(t)$, shown
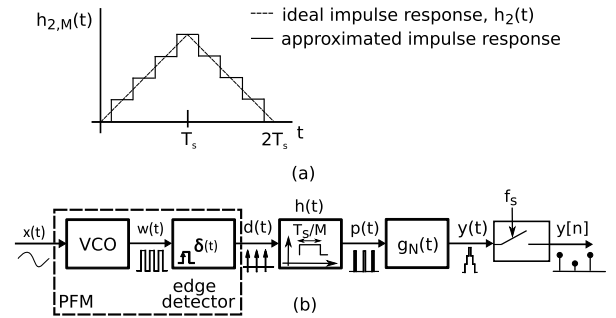

Fig. 18.   (a) Staircase approximation of the second order pulse shape and (b) a conceptual realization of the proposed idea which approximates second order spectral shaping.

in Fig. 18(a). Here, the staircase steps have a width of T_s/M and there are $2M - 1$ steps.

A conceptual realization of this idea is shown in Fig. 18(b). Here, the signal $d(t)$ coming from the PFM is filtered by a filter with impulse response $h(t)$ consisting of a square pulse of length T_s/M (filter $h(t)$). The output $p(t)$ of this first filter is then applied to a second filter with impulse response $g_M(t)$. Finally the output $y(t)$ of this second filter is sampled to generate the final output data $y[n]$. The impulse response of the filter $h(t)$ can be written as:

$$h(t) = \frac{M}{T_s} \left(u(t) - u\left(t - \frac{T_s}{M} \right) \right) \qquad (16)$$

The second filter is a continuous time FIR filter [40] and its impulse response equals:

$$g_M(t) = \sum_{k=1}^{M} \left(k \cdot \delta\left(t - \left(k + \frac{1}{2} \right) \frac{T_s}{M} \right) \right) \\ + \sum_{k=1}^{M-1} \left((M-k) \cdot \delta\left(t - \left(M + k + \frac{1}{2} \right) \frac{T_s}{M} \right) \right) \qquad (17)$$

Now our staircase pulse shaper $h_{2,M}(t)$ of Fig. 18(a) can be written as:

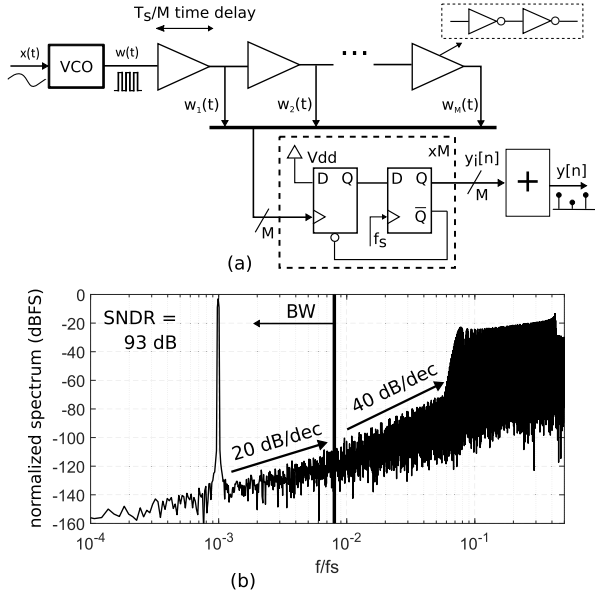$$h_{2,M}(t) = g_M(t) * h(t), \qquad (18)$$

Fig. 19. Practical implementation of the second order noise shaping approximation architecture: (a) circuit and (b) output spectrum for the case of a 256-tap approximation.

where $*$ stands for the convolution. In the Laplace domain this corresponds to:

$$H_{2,M}(s) = \frac{M}{T_s} \cdot \frac{1 - e^{-s\frac{T_s}{M}}}{s}$$
$$\cdot \sum_{k=1}^{M} \left(k \cdot e^{-s(k+\frac{1}{2})\frac{T_s}{M}} + (M-k) \cdot e^{-s(M+k+\frac{1}{2})\frac{T_s}{M}} \right)$$

(19)

If we calculate the limit when M approaches infinity, this becomes:

$$\lim_{M \to \infty} H_{2,M}(s) = \frac{1}{T_s^2} \cdot \frac{\left(1 - e^{-s \cdot T_s}\right)^2}{s^2} = H_2(s) \quad (20)$$

Therefore, the $sinc^2(f)$ filter is asymptotically approximated for a sufficiently large value of M. Consequently, increasing the number of steps in the staircase filter $g_M(t)$ will improve the performance of the system of Fig. 18(b) and bring it close to the ideal second order case.

For a practical realization of this idea, we can implement the analog FIR filter with a delay line composed of M delays elements [40], where each element introduces a delay of T_s/M. The proposed circuit is shown in Fig. 19(a). The implementation of such delay elements can be made with digital inverters or buffers that introduce a fixed continuous time delay in the digital signal. To understand that this circuit indeed implements the system of Fig. 18(b), we need to apply some transformations. First, we have to interchange the order of the $g_M(t)$ and $h(t)$ filters such that the FIR filter $g_M(t)$ comes first. Second, also the edge detection is shifted to the back and is performed implicitly in the first (left) flip-flop of Fig. 19(a). The validity of this transformation can be understood by observing that the edges of the VCO signal $w(t)$ are the same as the edges of the (theoretical) Dirac delta train signal $d(t)$, and this is still true after passing through the delay line. The actual sampling is performed by the second (right) flip flop in Fig. 19(b). Finally, the summation to implement

the overall filter is implemented after the sampling of every tap in the delay line.

Fig. 19(b) shows a simulation result for the implementation of Fig. 19(a). The simulation was made with a delay line with 256 taps. For the rest identical parameters were used as for the simulation of Fig. 12(b). Ideally this result should be very close to Fig. 12(b) and by a comparison of the two figures, we can see that this is true for a large part of the Nyquist band, where second-order noise shaping can clearly be observed. Also the corresponding SNDR of 93dB at an OSR=64 is very close to the ideal case. However, at very low frequencies the limitation of the approximation becomes visible and only first-order spectral shaping can be observed in this frequency range. Note that in this case, 8 output bits are needed to represent the output signal $y[n]$.

Also for this case, simulations with mismatch in the delay line were performed. For a mismatch up to 1% in the delay of each tap of the delay line, no performance degradation is observed. However, for higher mismatch, the performance starts to degrade.

In Fig. 19(a), we used a single-phase VCO. However, the approximation to the second order case can also be applied to multiphase VCOs if the delay line is connected to each phase of the VCO (e.g. signals $w_i(t)$ in Fig. 17).

At this point we should note the difference between the architectures depicted in Fig. 19(a) and Fig. 17. Both of them are multibit architectures, but how the multibit output signal is constructed is very different from each other. Firstly, the filter that shapes the pulse frequency modulated signal $d(t)$ is not the same for both cases (signal $d(t)$ in Fig. 19(a) would be the equivalent set of Dirac delta impulses obtained from signal $w(t)$). Whereas the pulse shaping filter for Fig. 19(a) is an approximation to a second-order sinc, the filter for Fig. 17 is a first-order sinc, regardless of the number of inverters in the ring oscillator. Consequently, we will not see second-order noise-shaping in the output spectrum of Fig. 17. Secondly, the delays of the inverters in the delay line of Fig. 19(a) are constant and signal independent as we want to implement a time invariant FIR filter. However, in a ring oscillator the inverter delays are modulated by the input signal $x(t)$, as described in the equivalent model of Fig.17(b) where the multiplexer advancement depends on the input signal $d(t)$. As depicted in Fig. 16(d), the high effective oscillation frequency makes the sampled output signal be multibit due to the overlapping between the pulses generated at the pulse shaping filters.

V. MASH VCO-BASED A/D CONVERSION

In the previous sections, a generic VCO-ADC architecture was described and the model of Fig. 11 was proposed to analyze the errors that occur in this architecture. In this section we will explain how two of our generic VCO-ADC's can be placed in a cascade configuration to form a MASH VCO-ADC. In principle the approach can be done for any order of the generic VCO-ADC. Nevertheless, we will limit the discussion to the case where the generic VCO-ADC is first order because this is the structure that can be implemented easily in practice. The resulting structure exhibits second order spectral shaping of the aliasing errors [2], [41].

A. 1-1 VCO-Based MASH Architecture

The operating principle of our proposed MASH architecture can be understood from the model shown in Fig. 20. It consists
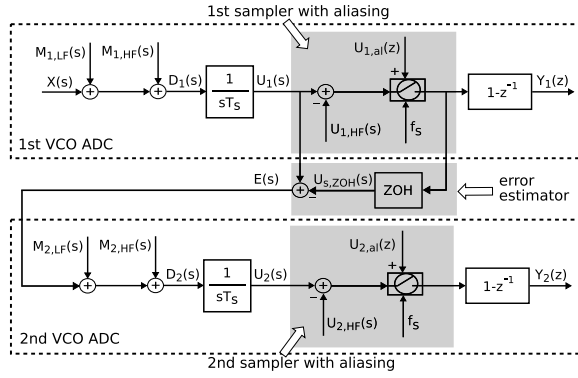
Fig. 20. Model describing the proposed 1-1 VCO-based MASH.

of a first VCO-ADC, an error estimator block and a second VCO-ADC. In the figure, each VCO-ADC is modeled according to the previously derived model of Fig. 11. As before, to simplify the discussion, the VCO gains were normalized to unity and the offset contributions corresponding to the VCO rest oscillation f_o were omitted.

On the top-level, the architecture is similar to typical continuous-time MASH $\Delta\Sigma$ modulators [42], [43], which also consist of a first ADC, an error estimator and a second ADC. However, in our case, no conventional analog blocks (such as opamps, comparators, …) are used, only VCOs and digital circuitry. The first VCO-ADC is driven by the overall input signal $X(s)$ and produces a digital, discrete time output signal $Y_1(z)$. From the analysis above, we know that:

$$Y_1(z) = \left[\text{STF}\,(X(s) + M_{1,\text{LF}}(s))\right]^* + U_{1,\text{al}}(z)(1 - z^{-1}) \quad (21)$$

where the aliased modulation component $U_{1,\text{al}}(z)$ is given by:

$$U_{1,\text{al}}(z) = \left[\frac{M_{1,\text{HF}}}{sT_s}\right]^* \quad (22)$$

In practice the performance is limited by the first order differentiated contribution of $U_{1,\text{al}}(z)$.

The key enabling element in our proposed structure is the error estimator block, which generates a continuous time signal $e(t)$. Signal $e(t)$ is an estimation of the dominant first stage's error. Since this error is the aliasing error $U_{1,\text{al}}(z)$ which occurs in the sampler, the error signal can be obtained by taking the difference between the sampler's input and its output, as shown in Fig. 20. To be more precise, we can write E as:

$$E = U_{1,\text{LF}} + U_{1,HF} - \left[U_{1,\text{LF}}\right]^* H_{\text{ZOH}} - U_{1,\text{al}}(z)H_{\text{ZOH}} \quad (23)$$

where $U_{1,\text{LF}}$ and $U_{1,\text{HF}}$ are defined as follows:

$$U_1 = U_{1,\text{LF}} + U_{1,\text{HF}} \quad (24)$$

with

$$U_{1,\text{LF}} = \frac{X + M_{1,\text{LF}}}{sT_s} \quad (25)$$

$$U_{1,\text{HF}} = \frac{M_{1,\text{HF}}}{sT_s} \quad (26)$$

Here, abstraction is made from the transform domain (either frequency domain or s-domain), and we are implicitly assuming that the s-domain representation of the 'z'-variable is e^{sT_s}.

As before the subscript $_{\text{LF}}$ denotes low frequency components that are not prone to aliasing. The transfer function H_{ZOH} corresponds to the zero order hold pulse and equals $(1 - e^{-sT_s})/(sT_s)$. Clearly when taking into account that for low frequencies $H_{\text{ZOH}} \approx 1$, we immediately see that the low frequency component E_{LF} of our error estimation E corresponds to the aliasing error:

$$E_{LF} \approx -U_{1,\text{al}},$$

which is the desired behavior. This error signal E drives the second VCO and hence, in a similar way as for (21), we can write:

$$Y_2(z) = \left[\text{STF}\,(E(s) + M_{2,\text{LF}}(s))\right]^* + U_{2,\text{al}}(z)(1 - z^{-1}) \quad (27)$$

Now, the core idea of a MASH structure is to pass each stage's output through proper noise cancellation filters (NCFs) and combining them into the overall output signal $Y(z)$. If done appropriately, the error from the first stage is removed and overall higher noise shaping order is achieved. The most obvious choice for the noise cancellation filters NCF_1 and NCF_2 is[3]:

$$NCF_1 = 1 \qquad NCF_2 = 1 - z^{-1} \quad (28)$$

Then the overall output signal $Y(z)$ is obtained as:

$$Y(z) = NCF_1 \cdot Y_1(z) + NCF_2 \cdot Y_2(z)$$
$$= Y_1(z) + (1 - z^{-1}) \cdot Y_2(z) \quad (29)$$

If we now make the approximation that the filter effect of the Zero Order hold pulse is negligible we can write the overall output as:

$$
\begin{aligned}
Y(z) \approx\ & [\text{STF} \cdot X(s)]^* \\
& + \left[\text{STF} \cdot M_{1,\text{LF}}(s)\right]^* \\
& + \left(1 - z^{-1}\right) \cdot [1 - \text{STF}]^* \cdot U_{1,\text{al}}(z) \\
& + \left(1 - z^{-1}\right) \cdot \left[\text{STF} \cdot M_{2,\text{LF}}(s)\right]^* \\
& + \left(1 - z^{-1}\right)^2 \cdot U_{2,\text{al}}(z) \quad (30)
\end{aligned}
$$

In the above expression, we can make the further approximation that in the signal band the signal transfer function STF is approximately unity. Then the expression can be further simplified into:

$$
\begin{aligned}
Y(z) \approx\ & [X(s)]^* + \left[M_{1,\text{LF}}(s)\right]^* \\
& + \left(1 - z^{-1}\right) \cdot \left[M_{2,\text{LF}}(s)\right]^* \\
& + \left(1 - z^{-1}\right)^2 \cdot U_{2,\text{al}}(z) \quad (31)
\end{aligned}
$$

From this expression we see that there are three terms that can degrade the performance. First, there is the contribution from $M_{1,\text{LF}}$, the fundamental PFM encoding error of the first stage (see Fig. 7). The way to keep this error contribution under control is to limit the input signal amplitude and to operate the first VCO at a sufficiently high effective oscillation frequency. Second, there is a contribution from $M_{2,\text{LF}}$, the fundamental PFM encoding error of the second stage. This contribution is first order differentiated, and hence should not limit the performance. However, the input of the second VCO

[3]If we work with non unity values of K_{VCO} appropriate gain factors should be added to the noise cancellation filters.
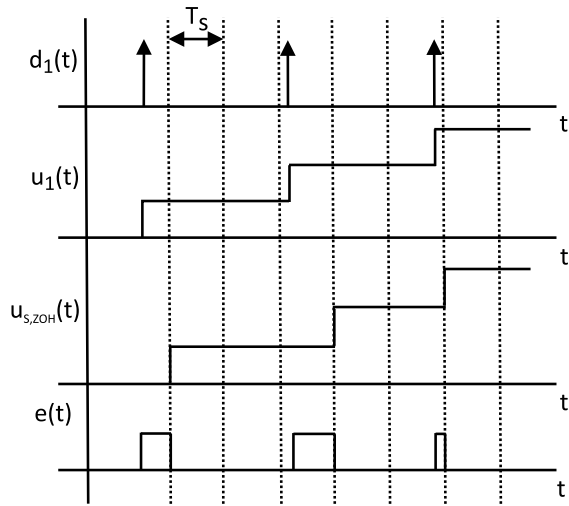
Fig. 21. Time domain waveforms of the relevant signals to obtain the error estimation $e(t)$ in a VCO-based stage.

is the error signal whose amplitude is large, which is not a favorable situation for this error contribution (see Fig. 7). Hence, to keep this error contribution under control the second VCO should be operated at a sufficiently high effective oscillation frequency. Finally, there is the second stage aliasing error. If the appropriate measures are taken to limit the fundamental PFM encoding error terms, (31) can be further simplified into:

$$Y(z) \approx [X(s)]^* + \left(1 - z^{-1}\right)^2 \cdot U_{2,\text{al}}(z) \qquad (32)$$

In this expression we see that the limiting factor is formed by the second stage aliasing error, but this error exhibits a second-order spectral shaping.

B. Practical Implementation

The key element in the practical implementation is the error estimator block. In order to better understand its operation, Fig. 21 shows the relevant time domain waveforms: i.e. $d_1(t)$, $u_1(t)$, the sampled and held version of $u(t)$ ($u_{\text{s,ZOH}}(t)$) and the error signal $e(t)$ for the case of a single-phase VCO. From the figure it is clear that the error signal $e(t)$ is always discrete in amplitude, and hence can be implemented with digital circuitry.

The error estimator circuit can be combined with the efficient (and almost standard practice) circuit of Fig. 1(a). In this case, if the following condition relative to the maximum oscillation frequency in the first VCO is accomplished:

$$f_{1,max} \leq \frac{f_s}{2} \qquad (33)$$

the signal $e(t)$ is even a two-level (single-bit) signal.

The proposed implementation is shown in Fig. 22 for the generic case of a M-phases VCO in the first stage. At the moment, we will focus on the case in which $M=1$. By drawing the waveforms for this circuit under the condition (33), it is immediately verified that signal $e(t)$ is identical to the desired waveform of Fig. 21, which confirms the correct operation of the circuit. This configuration has an additional advantage: the second VCO is driven by a 1-bit signal and hence will always operate linearly at two possible oscillation frequencies [44].
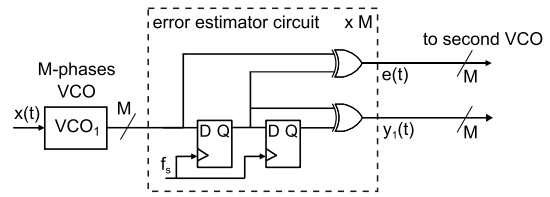

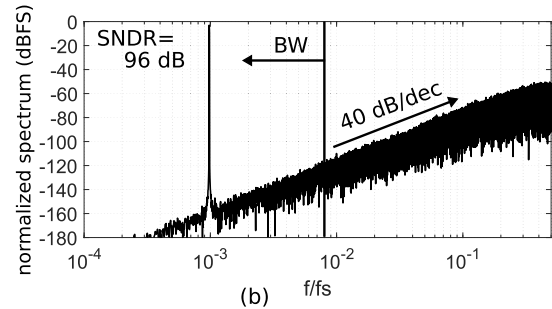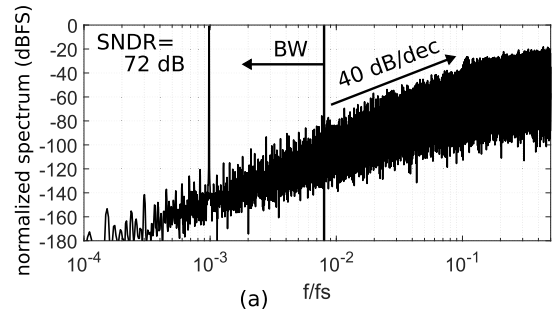Fig. 22. Practical implementation of the error estimator circuit with a M-phases VCO.

Fig. 23. VCO-based MASH output spectrum with: (a) single-phase VCOs, and (b) multiphase VCOs ($M = 15$).

To confirm the performance of this structure, several behavioral simulations were performed. Fig. 23(a) shows a typical resulting output spectrum. The simulation was done with the following VCO parameters:

$$f_1 = f_{o,1} + K_{\text{VCO},1} \cdot x(t) = \frac{f_s}{4} + \frac{f_s}{4} \cdot x(t) \qquad (34)$$

$$f_2 = f_{o,2} + K_{\text{VCO},2} \cdot e(t) = \frac{f_s}{4} + \frac{f_s}{4} \cdot e(t) \qquad (35)$$

Here the two digital levels of $e(t)$ correspond to the signal values $e = -1$ and $e = 1$ and, as before, the input signal $x(t)$ is scaled such that it is in the interval [-1,1]. The input signal was a -3 dBFS sinusoid with a signal frequency $f_x = f_s/1024$. The plot clearly demonstrates second-order spectral shaping. For an OSR=64, the SNDR is 72 dB. This performance seems modest compared to the performance demonstrated in the second-order case of Fig. 12(b) and the (approximately) second order case of Fig. 19, where the SNDR was respectively 95 dB and 93 dB for the same OSR. However, it is important to note that both y_1 as well as y_2 are single bit signals, whereas the output signal for the theoretical case of Fig. 12(b) was a real number that cannot be represented with a finite number of bits, and the output signal for the case of Fig. 19 was an 8-bit signal.

The extension to the multiphase case can be built by replicating the error estimator circuit for each of the phases in the first VCO (as shown in Fig. 22) and combining all of the error signals into a multibit signal. Then, the second VCO works as a digital controlled oscillator. Fig. 23(b) shows a simulation of the MASH architecture implemented with 15-phases VCOs,
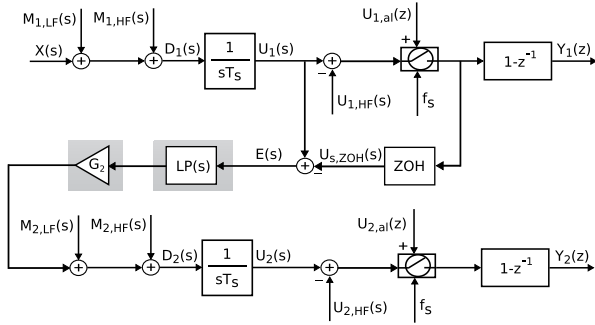
Fig. 24. Linear model for the proposed 1-1 VCO-based-MASH incorporating finite coupling bandwidth and gain mismatch in the second VCO.

both in the first and the second stage. With similar parameters to Fig. 23(a) the SNDR is 96 dB, approximately the same as in Fig. 19(b).

C. Finite Interconnection Bandwidth and Gain Mismatch

There are two important performance limiting factors in the practical implementation described above: i.e. interconnection bandwidth and VCO gain mismatch in the second VCO. Both are illustrated in Fig. 24. The analyzed limiting factors apply similarly to both single-phase and multiphase cases.

The interconnection bandwidth issue is associated to the xor-gate that generates the error signal $e(t)$ (see Fig. 22). This gate has to drive the load formed by the input impedance of the second VCO. However, it cannot produce infinitely steep edges, which were implicitly assumed in the discussion above (see the waveforms in Fig. 21). To model this effect, the bandwidth limiting low-pass filter $LP(s)$ is inserted in Fig. 24. In addition to the finite coupling bandwidth, the gain of the second VCO ($K_{VCO,2}$) cannot be controlled with an infinite accuracy. Due to this, the actual gain of the second VCO will always deviate from the desired value. To take this effect into account a gain mismatch coefficient G_2 was added to the model. When we analyze these effect and make the same approximations as in the derivation of (31), we come to the conclusion that the actual conversion result $Y'(z)$ is now:

$$Y'(z) = Y(z) + U_{1,leak}, \qquad (36)$$

where $Y(z)$ stands for the ideal conversion result of (31) and $U_{1,leak}$ corresponds to a leakage term which, within the approximations that were used to obtain (31), can be found as:

$$U_{1,leak} = [1 - G_2 \cdot LP(s) \cdot STF]^* \cdot \left(1 - z^{-1}\right) U_{1,al}(z) \quad (37)$$

Note that such a leakage effect is very similar to what occurs in other types of MASH converters [45], [46].

VI. CONCLUSION

This paper shows a novel methodology to analyze and design VCO-ADCs with extended noise shaping properties. The key element of the approach is that the VCO is considered as a signal encoder, instead of the typical interpretation where the VCO is viewed as a phase integrator. For this, an exact equivalence between a PFM and a VCO is established. This equivalence allows to reveal the fundamental PFM encoding error which forms an ultimate limitation of any VCO-ADC and which was quantified in Fig. 7.

In a next step, we used the PFM interpretation for a direct construction of the generic VCO-ADC of Fig. 8. We have shown that the noise shaping order of this VCO-ADC architecture is determined by the filter that shapes the modulation components of the VCO. Ideally, if the correct filter was chosen, any noise shaping order architecture could be designed. Whereas the version with first order spectral turns out to be easy to implement, unfortunately, the ideal high order variants turn out to be complicated to implement in practice. As a partial solution for this limitation, we have proposed a practical technique to approximate the second order case through the use of a FIR filter composed of a delay line.

Finally, we extended these results to a multistage (MASH) architecture for which we proposed the very simple implementation of Fig. 22. Based on the PFM interpretation, we could show analytically that this structure allows second order spectral shaping, which was confirmed by simulations.

REFERENCES

[1] M. Hovin, A. Olsen, T. S. Lande, and C. Toumazou, "Delta-sigma converters using frequency-modulated intermediate values," in *Proc. IEEE Int. Symp. Circuits Syst. (ISCAS)*, vol. 1. Apr. 1995, pp. 175–178.

[2] M. Hovin, A. Olsen, T. S. Lande, and C. Toumazou, "Delta-sigma modulators using frequency-modulated intermediate values," *IEEE J. Solid-State Circuits*, vol. 32, no. 1, pp. 13–22, Jan. 1997.

[3] B. Murmann. *ADC Performance Survey 1997–2017*. [Online]. Available: http://web.stanford.edu/~murmann/adcsurvey.html

[4] U. Wismar, D. Wisland, and P. Andreani, "A 0.2V 0.44 µW 20 kHz analog to digital Σ∆ modulator with 57 fJ/conversion FoM," in *Proc. ESSCIRC*, Sep. 2006, pp. 187–190.

[5] T. Watanabe and T. Terasawa, "An all-digital ADC/TDC for sensor interface with TAD architecture in 0.18-µm digital CMOS," in *Proc. 16th IEEE Int. Conf. Electron., Circuits Syst. (ICECS)*, Dec. 2009, pp. 219–222.

[6] J. Kim, T. K. Jang, Y. G. Yoon, and S. Cho, "Analysis and design of voltage-controlled oscillator based analog-to-digital converter," *IEEE Trans. Circuits Syst. I, Reg. Papers*, vol. 57, no. 1, pp. 18–30, Jan. 2010.

[7] L. B. Leene and T. G. Constandinou, "Time domain processing techniques using ring oscillator-based filter structures," *IEEE Trans. Circuits Syst. I, Reg. Papers*, to be published. [Online]. Available: http://ieeexplore.ieee.org/document/7971944/

[8] A. Babaie-Fishani and P. Rombouts, "A mostly digital VCO-based CT-SDM with third-order noise shaping," *IEEE J. Solid-State Circuits*, vol. 52, no. 8, pp. 2141–2153, Aug. 2017.

[9] S. Rao, B. Young, A. Elshazly, W. Yin, N. Sasidhar, and P. K. Hanumolu, "A 71dB SFDR open loop VCO-based ADC using 2-level PWM modulation," in *Symp. VLSI Circuits-Dig. Tech. Papers*, Jun. 2011, pp. 270–271.

[10] M. Park and M. H. Perrott, "A 78 dB SNDR 87 mW 20 MHz bandwidth continuous-time ∆Σ ADC with VCO-based integrator and quantizer implemented in 0.13 µm CMOS," *IEEE J. Solid-State Circuits*, vol. 44, no. 12, pp. 3344–3358, Dec. 2009.

[11] J. Daniels, W. Dehaene, M. Steyaert, and A. Wiesbauer, "A 0.02 mm² 65 nm CMOS 30 MHz BW all-digital differential VCO-based ADC with 64 dB SNDR," in *Proc. Symp. VLSI Circuits*, Jun. 2010, pp. 155–156.

[12] M. Voelker, S. Pashmineh, J. Hauer, and M. Ortmanns, "Current feedback linearization applied to oscillator based ADCs," *IEEE Trans. Circuits Syst. I, Reg. Papers*, vol. 61, no. 11, pp. 3066–3074, Nov. 2014.

[13] E. Gutierrez, L. Hernandez, U. Gaier, S. Walter, and L. Zou, "A low power and low distortion VCO based ADC using a pulse frequency modulator," in *Proc. IEEE 57th Int. Midwest Symp. Circuits Syst. (MWSCAS)*, Aug. 2014, pp. 487–490.

[14] A. Ghosh and S. Pamarti, "Linearization through dithering: A 50 MHz bandwidth, 10-b ENOB, 8.2 mW VCO-based ADC," *IEEE J. Solid- State Circuits*, vol. 50, no. 9, pp. 2012–2024, Sep. 2015.

[15] A. Babaie-Fishani and P. Rombouts, "Highly linear VCO for use in VCO-ADCs," *Electron. Lett.*, vol. 52, no. 4, pp. 268–270, 2016.

[16] A. Babaie-Fishani and P. Rombouts, "Design of a low-voltage op-amp-less ASDM to linearise VCO-ADC," *Electron. Lett.*, vol. 52, no. 11, pp. 911–913, May 2016.

[17] L. Hernández, "VCO based multi-stage noise shaping ADC," *Electron. Lett.*, vol. 48, no. 4, pp. 206–208, Feb. 2012.

[18] A. Wiesbauer, D. Straussnigg, L. Hernandez, and F. Cardes, "System and method for an oversampled data converter," U.S.Patent 2014 0 270 261, Sep. 18, 2014.

[19] W. Yu, J. Kim, K. Kim, and S. Cho, "A time-domain high-order MASH ΔΣ ADC using voltage-controlled gated-ring oscillator," *IEEE Trans. Circuits Syst. I, Reg. Papers*, vol. 60, no. 4, pp. 856–866, Apr. 2013.

[20] Y. Yoon, K. Lee, P. Wang, and N. Sun, "A purely-VCO-based single-loop high-order continuous-time ΣΔ ADC," in *Proc. IEEE Int. Symp. Circuits Syst. (ISCAS)*, Jun. 2014, pp. 926–929.

[21] A. Babaie-Fishani and P. Rombouts, "True high-order VCO-based ADC," *Electron. Lett.*, vol. 51, no. 1, pp. 23–25, 2015.

[22] A. Sanyal and N. Sun, "Second-order VCO-based ΔΣ ADC using a modified DPLL," *Electron. Lett.*, vol. 52, no. 14, pp. 1204–1205, Jul. 2016.

[23] M. Park and M. H. Perrott, "A VCO-based analog-to-digital converter with second-order Sigma-Delta noise shaping," in *Proc. IEEE Int. Symp. Circuits Syst.*, May 2009, pp. 3130–3133.

[24] U. Sönmez, F. Sebastiano, and K. A. A. Makinwa, "Analysis and design of VCO-based phase-domain ΣΔ modulators," *IEEE Trans. Circuits Syst. I, Reg. Papers*, vol. 64, no. 5, pp. 1075–1084, May 2017.

[25] S. Ardalan and J. Paulos, "An analysis of nonlinear behavior in delta-sigma modulators," *IEEE Trans. Circuits Syst.*, vol. CAS-34, no. 6, pp. 593–603, Jun. 1987.

[26] R. M. Gray, W. Chou, and P. W. Wong, "Quantization noise in single-loop sigma-delta modulation with sinusoidal inputs," *IEEE Trans. Commun.*, vol. 37, no. 9, pp. 956–968, Sep. 1989.

[27] C. M. Zierhofer, "Frequency modulation and first-order delta sigma modulation: Signal representation with unity weight dirac impulses," *IEEE Signal Process. Lett.*, vol. 15, pp. 825–828, 2008.

[28] M. Hovin, D. Wisland, Y. Berg, J. T. Marienborg, and T. S. Lande, "Delta-sigma modulation in single neurons," in *Proc. IEEE Int. Symp. Circuits Syst.*, vol. 5. May 2002, pp. V-617–V-620.

[29] L. Hernandez and E. Gutierrez, "Analytical evaluation of VCO-ADC quantization noise spectrum using pulse frequency modulation," *IEEE Signal Process. Lett.*, vol. 22, no. 2, pp. 249–253, Feb. 2015.

[30] E. Fitch, "The spectrum of modulated pulses," *J. Inst. Elect. Eng. IIIA, Radiocommun.*, vol. 94, no. 13, pp. 556–564, Mar./Apr. 1947.

[31] C. Wulff and T. Ytterdal, "Resonators in open-loop sigma–delta modulators," *IEEE Trans. Circuits Syst. I, Reg. Papers*, vol. 56, no. 10, pp. 2159–2172, Oct. 2009.

[32] C. M. Zierhofer, "Signal representation with unity-weight dirac impulses," *IEEE Trans. Signal Process.*, vol. 60, no. 6, pp. 2860–2869, Jun. 2012.

[33] E. J. Bayly, "Spectral analysis of pulse frequency modulation in the nervous systems," *IEEE Trans. Biomed. Eng.*, vol. BME-15, no. 4, pp. 257–265, Oct. 1968.

[34] S. Rao, K. Reddy, B. Young, and P. K. Hanumolu, "A deterministic digital background calibration technique for VCO-based ADCs," *IEEE J. Solid-State Circuits*, vol. 49, no. 4, pp. 950–960, Apr. 2014.

[35] G. Taylor and I. Galton, "A mostly-digital variable-rate continuous-time delta-sigma modulator ADC," *IEEE J. Solid-State Circuits*, vol. 45, no. 12, pp. 2634–2646, Dec. 2010.

[36] J. G. Tuxal, *Automatic Feedback Control System Synthesis*. New York, NY, USA: McGraw-Hill, 1955.

[37] S. Pavan, R. Schreier, and G. C. Temes, *Understanding Delta-Sigma Data Converters*. Hoboken, NJ, USA: Wiley, 2017.

[38] C. M. Zierhofer, "Quantization noise as superposition of frequency-modulated sinusoids," *IEEE Signal Process. Lett.*, vol. 16, no. 11, pp. 933–936, Nov. 2009.

[39] E. Gutierrez and L. Hernandez, "Spectral analysis of multibit VCO-ADCs and PFM-ADCs with sinusoidal inputs," in *Proc. IEEE Int. Symp. Circuits Syst. (ISCAS)*, May 2015, pp. 1258–1261.

[40] Y. Tsividis, "Mixing domains in signal processing," in *Proc. IEEE Int. Symp. Circuits Syst. (ISCAS)*, vol. 1. May 2004, pp. I-157–I-160.

[41] M. Finsrud, M. Hovin, and T. S. Lande, "Adaptive correction of errors in second-order MASH ΔΣ FDM solution," *IEEE Trans. Circuits Syst. II, Analog Digit. Signal Process.*, vol. 48, no. 11, pp. 1005–1013, Nov. 2001.

[42] D.-Y. Yoon, S. Ho, and H.-S. Lee, "An 85 dB-DR 74.6 dB-SNDR 50 MHZ-BW CT MASH ΔΣ modulator in 28 nm CMOS," in *IEEE ISSCC Dig. Tech. Papers*, Feb. 2015, pp. 1–3.

[43] L. J. Breems, R. Rutten, and G. Wetzker, "A cascaded continuous-time ΣΔ modulator with 67-dB dynamic range in 10-MHz bandwidth," *IEEE J. Solid-State Circuits*, vol. 39, no. 12, pp. 2152–2160, Dec. 2004.

[44] A. Elshazly, S. Rao, B. Young, and P. K. Hanumolu, "A noise-shaping time-to-digital converter using switched-ring oscillators—Analysis, design, and measurement techniques," *IEEE J. Solid-State Circuits*, vol. 49, no. 5, pp. 1184–1197, May 2014.

[45] A. Edward *et al.*, "A 43-mW MASH 2-2 CT ΣΔ modulator attaining 74.4/75.8/76.8 dB of SNDR/SNR/DR and 50 MHz of BW in 40-nm CMOS," *IEEE J. Solid-State Circuits*, vol. 52, no. 2, pp. 448–459, Feb. 2017.

[46] C. Zhang, L. J. Breems, G. Radulov, M. Bolatkale, H. Hegt, and A. van Roermund, "A digital calibration technique for wide-band CT MASH ΣΔ ADCs with relaxed filter requirements," in *Proc. IEEE Int. Symp. Circuits Syst. (ISCAS)*, May 2016, pp. 1486–1489.

Eric Gutierrez received the B.S. degree in industrial engineering and the M.S. degree in advanced electronic systems from the Carlos III University of Madrid, Madrid, Spain, in 2012 and 2014, respectively, where he is currently pursuing the Ph.D. degree in electrical engineering. He is also a Teaching Assistant with the Electronics Technology Department, Carlos III University of Madrid and as an External Consultant for Intel Austria GmbH, Villach, Austria. His interests are mixed-signal microelectronics, oversampled data converters, and biomedical instrumentation systems.

Luis Hernandez received the M.S. degree in telecommunication engineering and the Ph.D. degree from the Polytechnic University of Madrid, in 1989 and 1995, respectively. He did a post-doctoral research at Oregon State University, Corvallis, OR, USA, during 1996. In 1997, he joined the Electronics Technology Department, Carlos III University of Madrid, Madrid, Spain, where he is currently a Full Professor. His research has been focused in the field of analog microelectronics, specifically in data acquisition using sigma-delta modulation. He has authored over 100 papers. He holds 17 patents. He serves as a member of the IEEE Analog Signal Processing Technical Committee. Currently, he is an Associate Editor of the IEEE TRANSACTIONS ON CIRCUITS AND SYSTEMS I and a past Associate Editor of the IEEE TRANSACTIONS ON CIRCUITS AND SYSTEMS II.

Fernando Cardes received the B.S. degree in industrial electronics and automation engineering and the M.S. degree in advanced electronic systems from the Carlos III University of Madrid, Madrid, Spain, in 2012 and 2014, respectively. He is currently pursuing the Ph.D. degree with the Microelectronics Design and Applications Group, Electronics Technology Department, Carlos III University of Madrid. His research interests include mixed signal microelectronics, sensors, and instrumentation applications.

Pieter Rombouts was born in Leuven, Belgium, in 1971. He obtained the Ir. degree in applied physics and the Ph.D. degree in electronics from Ghent University in 1994 and 2000, respectively. Since 1994, he has been with the Electronics and Information Systems Department, Ghent University, where he has been a Professor of analog electronics since 2005. His technical interests are signal processing, circuits and systems theory, analog circuit design, and sensor systems. The main focus of his research has been A/D- and D/A-conversion. He has served or is currently serving as an Associate Editor of the IEEE TRANSACTIONS ON CIRCUITS AND SYSTEMS-I, the IEEE TRANSACTIONS ON CIRCUITS AND SYSTEMS-II, and *Electronics Letters*.